High spatial resolution microdosimetry with monolithic ΔE-E detector on ^{12}C beam: Monte Carlo simulations and experiment

Linh T. Tran [a,*], David Bolst [a], Susanna Guatelli [a], Giordano Biasi [d], Alberto Fazzi [d], Eleni Sagia [d], Dale A. Prokopovich [b], Mark I. Reinhard [b], Ying C. Keat [c], Marco Petasecca [a], Michael L.F. Lerch [a], Andrea Pola [d], Stefano Agosteo [d], Naruhiro Matsufuji [e], Michael Jackson [f], Anatoly B. Rosenfeld [a]

[a] *Centre for Medical Radiation Physics, University of Wollongong, NSW 2522, Australia*
[b] *NSTLI Nuclear Stewardship, Australian Nuclear Science and Technology Organization, Lucas Heights, NSW 2234, Australia*
[c] *University Sains Malaysia, Pulau Penang, Malaysia*
[d] *Dipartimento di Ingegneria Nucleare, Politecnico di Milano, 20133 Milano, Italy*
[e] *Research Centre for Charge Particle Therapy, National Institute of Radiological Science, Chiba, Japan*
[f] *University of New South Wales, Sydney, NSW 2052, Australia*

Nuclear fragmentation produced in ^{12}C ion therapeutic beams contributes significantly to the Relative Biological Effectiveness (RBE)—weighted dose in the distal edge of the Spread out Bragg Peak (SOBP) and surrounding tissues in out-of-field. Complex mixed radiation field originated by the therapeutic ^{12}C ion beam in a phantom is difficult to measure. This study presents a new method to characterise the radiation field produced in a ^{12}C ion beam using a monolithic ΔE-E telescope which provides the capability to identify the particle components of the mixed radiation field as well as the microdosimetric spectra that allows derivation of the RBE based on a radiobiological model. The response of the monolithic ΔE-E telescope to a 290 MeV/u ^{12}C ion beam at defined positions along the pristine Bragg Peak was studied using the Geant4 Monte Carlo toolkit. The microdosimetric spectra derived from the ΔE stage and the two-dimensional scatter plots of energy deposition in ΔE and E stages of the device in coincidence are presented, as calculated in-field and out-of-field. Partial dose weighted contribution to the microdosimetric spectra from nuclear fragments and recoils, such as ^{1}H, ^{4}He, ^{3}He, ^{7}Li, ^{9}Be and ^{11}B, have been analysed for each position. Comparison of simulation and experimental results are presented and demonstrates that the microdosimetric spectra changes dramatically within 0.5 mm depth increments close to and at the distal edge of the Bragg Peak which is impossible to identify using conventional Tissue Equivalent Proportional Counter (TEPC).

1. Introduction

Charged particle therapy with ^{12}C ions has the advantage over X-ray radiotherapy due to the Bragg Peak (BP) producing a highly conformal dose profile. Charged particle therapy is normally used for the treatment of deep-seated tumours while preserving the surrounding healthy tissues. The energy deposition mechanism of ions in matter is dominated by the electronic collisions for the relevant energies of primary ion, described by Bethe–Bloch formula [1,2]. The nuclear reactions contribute substantially to the ion dose via nuclear fragmentation and neutrons production. The determination of the Relative Biological Effectiveness (RBE) is crucial for particle therapy, particularly for heavier ions such as ^{12}C, as the biological dose is required as a parameter in patient treatment planning. Accurate knowledge of the RBE in-field and out-of-field is essential for determining the physical dose at a particular depth, D, to have the biological dose (RBED) constant along the SOBP, and to evaluate the secondary cancer risk and biological dose at Organs At Risk (OAR) out of the treatment field.

The RBE of a ^{12}C therapeutic beam changes dramatically with depth, especially towards the end of the Bragg Peak (BP) due to the very high Linear Energy Transfer (LET) of the ^{12}C ions in this region [3]. Additional complexity in the determination of the RBE in the target is associated with the nuclear fragmentation process in the SOBP. ^{12}C fragmentation produces lighter charged ions with lower LET than for primary ^{12}C ions as well as neutrons, which results in a slight reduction of the primary ^{12}C ions with increasing of the depth, as well as the production of a mixed radiation field which causes a low dose "tail" that extends beyond the distal edge of the SOBP [4]. The shape of the SOBP is formed by means of multiple pristine ^{12}C Bragg Peaks,

---

* Corresponding author.
E-mail addresses: tltran@uow.edu.au (L.T. Tran), anatoly@uow.edu.au (A.B. Rosenfeld).

Published Journal Article available at: https://doi.org/10.1016/j.nima.2017.12.079

which result in the formation of RBE ripples along the plateau of the SOBP.

An effective approach to derive the RBE for a ^{12}C ion beam is microdosimetry [5]. The microdosimetric approach involves measuring the frequency $f(y)$ of the stochastic lineal energy deposition y, in a micron sized tissue equivalent sensitive volume (SV). The lineal energy deposition y is defined as:

$$y = \frac{E}{\langle l \rangle}, \tag{1}$$

where E is the energy deposition in the SV, which has an average chord length $\langle l \rangle$. Once the microdosimetric spectra $y^2 f(y)$ vs y of a radiation field in tissue equivalent material is known, the RBE can be derived based on the modified microdosimetric-kinetic model (MKM) [6]. The RBE_{10} of the ^{12}C ion beam is defined as the ratio of the dose required to achieve 10% cell survival using X-rays to that required when using the radiation of interest:

$$\mathrm{RBE}_{10} = \frac{2\beta D_{10,R}}{\sqrt{\alpha^2 - 4\beta ln\,(0.1)} - \alpha}, \tag{2}$$

where α, β are individual tissue radiosensitivity coefficients (α, in units of Gy^{-1} and β, in units of Gy^{-2}) determined the cell survival, $D_{10,R} = 5.0$ Gy is the dose corresponding to 10% survival for human salivary gland (HSG) cells using 200 kVp X-rays as reference radiation. α is defined as:

$$\alpha = \alpha_o + \frac{\beta}{\rho \pi r_d^2} y^* \tag{3}$$

where $\alpha_0 = 0.13\ \mathrm{Gy}^{-1}$ is a constant that represents the initial slope of the survival fraction curve in the limit of zero LET, $\beta = 0.05\ \mathrm{Gy}^{-2}$ is a constant independent of LET, $\rho = 1\ \mathrm{g/cm}^3$ is the density of tissue and $r_d = 0.42$ μm is the radius of a sub-cellular domain in the MK model.

$$y^* = \frac{y_o^2 \int_0^\infty \left(1 - exp\left(-y^2/y_o^2\right)\right) f(y)\, dy}{\int_0^\infty y f(y)\, dy}, \tag{4}$$

where $y_o = 150$ keV/μm is used in this study in order to match the calculation method used at the Heavy Ion Medical Accelerator in Chiba (HIMAC) in experiments with the tissue equivalent proportional counter (TEPC).

The Centre for Medical Radiation Physics (CMRP), University of Wollongong, has initiated the concept of silicon microdosimetry to replace the current microdosimetry gold standard, the TEPC. Compared to the TEPC, silicon microdosimeters are advantageous due to being a solid-state detector with no gas-flow ensemble, having very low operating voltages less than 10 V, extremely high spatial resolution (μm scale) and a high degree of portability. Current status of silicon microdosimetry can be found elsewhere [7].

The characteristics of secondary charged particles in ^{12}C ion beams of 200 and 400 MeV/u have been previously studied using the combination of energy loss and time-of-flight (TOF) measurements. A thin scintillation paddle with 1.5 mm thick coupled to a Hamamatsu photomultiplier tube was used [8]. The monolithic ΔE–E telescope with 1.8 μm thick ΔE stage can be used at the same time as a microdosimeter and as detector to identify products deriving from nuclear fragmentation [9,10].

The latest design of the monolithic telescope has a pixelated ΔE detector with SVs similar in geometry to CMRP SOI microdosimeters [7,11]. The pixelated ΔE stage allows the device to be used as a microdosimeter while also providing particle identification [12].

The ΔE–E telescope was used earlier to derive the RBE based on the microdosimetric approach, at defined positions along and downstream of a 100 MeV pristine proton Bragg peak and including distal part of SOBP at the proton therapy facility at Loma Linda University [13]. It was demonstrated that the maximum RBE value did not coincide with the physical dose peak position but was slightly downstream of the distal edge of the Bragg Peak. The study showed that the RBE varied with the depth along the SOBP and was higher than the RBE value being used in proton treatment planning (equal to a constant value of 1.1 along the SOBP). This was in agreement with currently published experimental microdosimetry based derived RBE obtained with high spatial resolution in therapeutic proton beams [14].

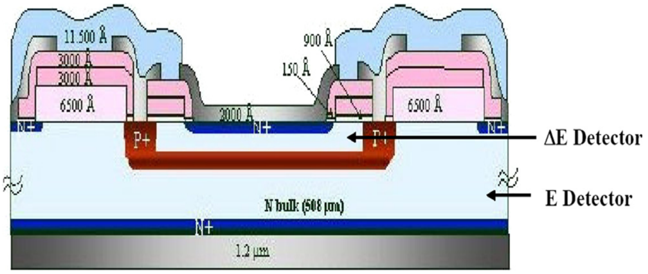

Fig. 1. Schematic of ΔE–E telescope.
Source: Figure adapted from [14].

We are currently investigating the use of the ΔE–E monolithic telescope for RBE determination both in-field and out-of-field of the ^{12}C ion beam field. The project involved experimental characterisation of the device at the HIMAC facility, Chiba, Japan, coupled with Geant4-based simulation studies.

In this paper we present the response of the ΔE–E telescope in-field and out-of-field of a 290 MeV/u^{12}C beam simulated by Geant4 to justify application of the ΔE–E telescope as a high spatial resolution Quality Assurance (QA) tool in heavy ion therapy (HIT). The simulation results are compared to experimental measurements performed at HIMAC, to have a first indication on the accuracy of the Geant4 simulation model. Particular attention was devoted to the study of the ^{12}C fragmentation and neutrons contribution to the derived RBE in the distal part and downstream of the Bragg peak.

2. Materials and methods

2.1. ΔE–E telescope system description

The monolithic ΔE–E monolithic telescope, manufactured at ST Microelectronics (Catania, Italy), consists of a 1.8 μm ΔE and a 500 μm E thick stage, both manufactured on a single silicon substrate. The detector response can be presented as a two-dimensional scatter plot of the ΔE vs ΔE + E energy deposition via coincidence data acquisition.

A schematic of the ΔE–E telescope is shown in Fig. 1, where thin metallised N^+ implanted $n - p$ junctions for both ΔE and E detectors are depleted towards a P^+ buried anode which is a common ground contact separating the two stages of the detector. To fully deplete the particle telescope the N^+ contact ΔE was biased at +5 V and the N^+ contact of the E stage was biased at +100 V relative to the P^+ buried layer.

The ΔE–E particle telescope can be operated in a number of modes by utilising the ΔE and E detectors separately or in coincidence. When operated separately, the ΔE detector acts like a microdosimeter in the case when the charged particle beam is normally incident to the surface of the detector. The mean chord length is defined by the thickness of the ΔE detector (1.8 μm) for normally incident radiation.

2.2. Geant4 simulation application

The Geant4 version 4.9.6.p01 [15] was used to model the radiation field and the response of the ΔE–E telescope to a 290 MeV/u ^{12}C beam in a PMMA phantom.

The experimental setup of the simulation, illustrated in Fig. 2, reflected the experimental conditions of the measurements performed at HIMAC. The ^{12}C ion beam was simulated with an area of $1 \times 1\ \mathrm{mm}^2$ and the distance from the ion beam line exit window to the surface of the phantom was 10 m as shown in Fig. 2. A 0.4 mm thick lead

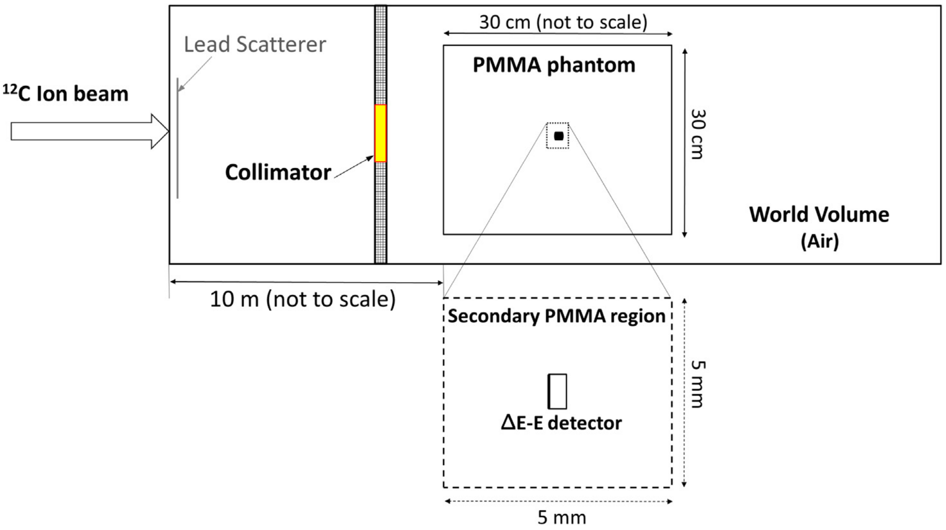

Fig. 2. Schematic representation of the simulated geometry of ΔE–E telescope in the Geant4 simulation.

scatterer, placed at 5 mm from the ion beam line exit window, was used for beam scattering. A 50 mm thick brass collimator with 10×10 cm^2 square aperture was placed at 30 cm from the surface of the phantom. The mixed radiation field produced by the incident ^{12}C ion beam was studied in the PMMA phantom, modelled as a $30 \times 30 \times 30$ cm^3 box, with elemental composition taken from ICRU [16] and with a density of 1.17 g/cm^3.

The electromagnetic interactions of particles were described by means of the Geant4 Standard Physics Package (*G4EmStandardPhysics_option3*). The hadronic interactions were described by means of the *QGSP_BIC_HP* physics list. Ion nuclear interactions were modelled with the *G4IonBinaryCascadeModel*.

In the first part of the study, the mixed radiation field deriving from the ^{12}C ion beam was characterised. The output of the simulation consisted of the energy deposition in the PMMA phantom as well as the position of secondary particles generated within the phantom. The energy deposition derived from the incident primary beam and from the secondary nuclear fragments was tallied separately. The Bragg Peak was calculated along the direction of the incident beam with 0.1 mm spatial resolution. The deposited energy at a given depth on a beam central axis and laterally was stored in the 2D histogram which had 1 mm^2 pixels.

In the second part of the study, the response of the ΔE–E telescope to a 290 MeV/u ^{12}C beam was modelled to verify the capability of this device in identifying different nuclear fragments in-field and out-of-field.

The geometry of the ΔE and E stages was modelled as 1 mm × 1 mm × 1.8 μm and 1 mm × 1 mm × 500 μm silicon slabs. The ΔE–E telescope was placed in the PMMA phantom at different depth. The Geant4 *cuts per region* [17] were used to reduce the simulation times without affecting the accuracy of the results. The size of the region was chosen based on a conservative consideration of the range of secondary electrons produced by the primary ^{12}C ion beam field. The maximum range of delta electrons produced by a 290 MeV/u ^{12}C was approximately 2.4 mm in PMMA (NIST database [18]). Based on these considerations the region was centred with the detector, with a lateral size of 5 mm to track all δ-electrons at the required accuracy in the surrounding ΔE–E telescope. The range cut was set low enough to track the δ-electrons down to the low energy limit of the Geant4 Standard Electromagnetic Physics of 1 keV. Outside the region, the cut was set to 2 mm to reduce computation time because those δ-electrons with a range smaller than 2 mm cannot reach the ΔE–E telescope.

Fig. 2 Shows the simulated experimental set-up. The energy deposition was calculated per incident particle on the device, depositing energy in both ΔE and E stages (coincidence mode). The energy deposition caused by δ-electrons and other secondary particles originating inside the two detector stages was assigned to the parent particle incident on the device. The kinetic energy, charge, and baryon number of the particle producing the energy deposition event in the device were scored

The in-field and out-of-field response of the ΔE–E telescope was obtained at 15 positions along the axis of irradiation, that is: 0, 10, 58, 106, 125, 126.5, 127, 128, 128.5, 129.5, 130, 131.5, 136.5, 141, and 155 mm. These positions were selected to encompass both in-field and downstream of the Bragg Peak measurements as well as to match the experimental measurement positions.

The out-of-field response of the ΔE–E telescope was studied to characterise composition of the mixed radiation field, including the scattered primary ion beam, fragments and neutrons which are needed to estimate the stochastic probability of secondary cancer induction. The out-of-field study was done with the ΔE–E telescope facing the ^{12}C ion beam (face on 0°) and edge on (90°) as shown in Fig. 3. The ΔE–E telescope was placed at 0 mm, 2 mm, 7 mm and 47 mm laterally from the edge of the radiation field at the Bragg Peak region (for both cases: “face on” noted as F and “edge on” noted as E).

3. Results and discussion

3.1. Characterisation of ^{12}C ion beam mixed radiation field

Fig. 4a shows the energy deposited by the incident 290 MeV/u ^{12}C ions and by the secondary fragment particles. A Bragg Peak was observed at (129.5 ± 0.1) mm in the PMMA phantom which agrees with calculated results by SRIM [19]. The main contribution to the total energy deposition derived from the incident ^{12}C ion beam, fragments, neutrons and the secondary carbon ions. Secondary carbon ions resulted mostly from neutron elastic scattering within the PMMA. Such secondary carbon ions are absent in the case of a water phantom. The peak of the secondary carbon ion appeared at 120 mm in the PMMA phantom (Fig. 4b). Contributions to the total energy deposition were seen from secondary nuclei, due to recoils, namely H, He, Li, Be, B, N, and O. The almost negligible energy deposition contributed by N and O was not included in Fig. 4b.

Table 1 shows the number of secondary fragments generated per single incident ^{12}C ion and indicate that protons possess the highest yield. These protons are fragmented protons as well as recoil protons generated in elastic reactions when the neutrons interacted with the hydrogen nuclei in the PMMA material. The second largest secondary particle yield was from secondary C followed by neutron, O, He, B, Li, N and Be ions.

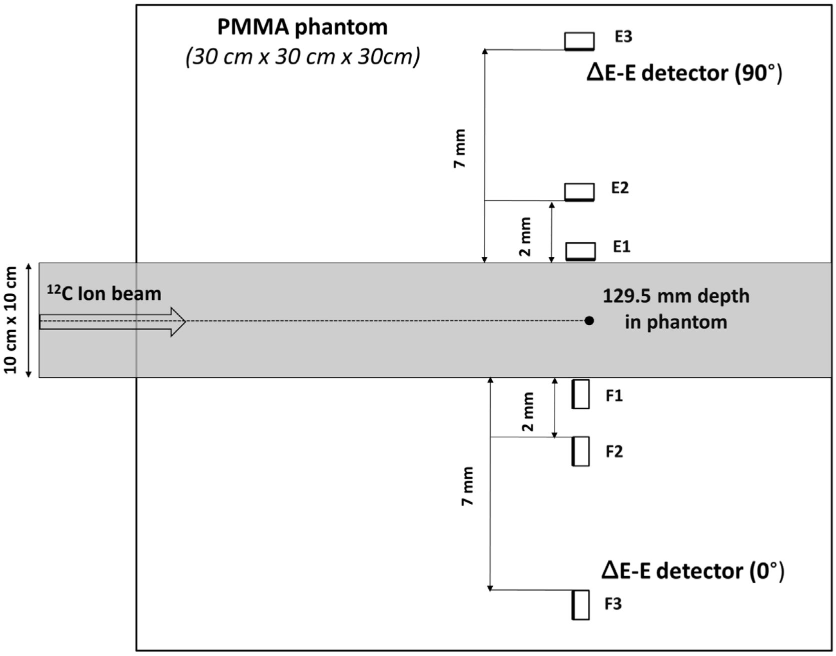

Fig. 3. Schematic representation of out of field positions of the ΔE–E telescope in the Geant4 simulations and experiments (not to scale). Positions F4 and E4 corresponding to 47 mm lateral distance from the edge of the radiation field are not shown due to space limitation.

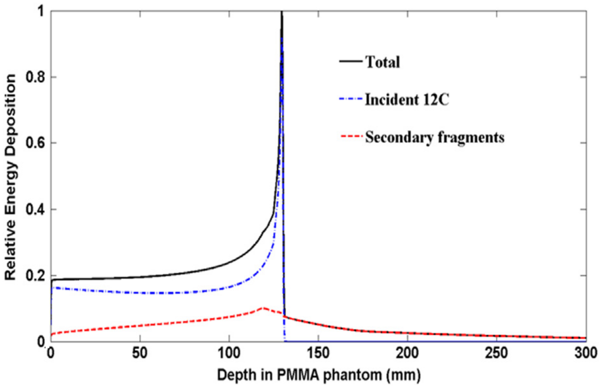

Fig. 4a. Dose per incident ^{12}C ions. The contribution deriving from incident ^{12}C ions and secondary fragments are shown in blue and red, respectively. The sum of the two contributions is shown with the black curve. The energy deposition at the BP was normalised to 1. (For interpretation of the references to colour in this figure legend, the reader is referred to the web version of this article.)

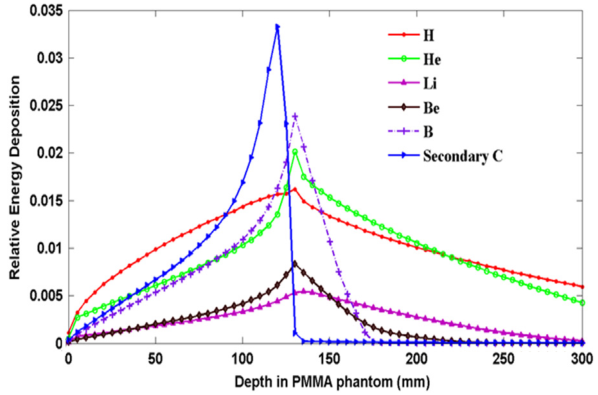

Fig. 4b. Energy deposition n deriving from the most significant secondary nuclear fragments and recoil secondary carbon ions (non-primary carbon ions). The total energy deposited by the secondary fragments component was normalised to 1.

Table 1
Number of secondary particles produced per single incident ^{12}C ion.

Particle	Production per single ^{12}C
H	25.33
Secondary C	4.26
Neutron	2.37
O	1.48
He	1.29
B	0.49
Li	0.24
N	0.16
Be	0.14

Fig. 5 shows the 2D energy distribution from primary and secondary particles in the PMMA phantom. Two additional lines were added to mark the edges of the primary beam (10 cm × 10 cm) and range of the primary carbon ions. The 2D histogram shows the minimal scattering of the primary ^{12}C ions outside the radiation field that confirm the advantage of HIT with a sharp penumbra. All fragmented ions are producing dose buildup towards the end of the Bragg peak as demonstrated in Figs. 4b and 5. Fragmented C, O, B, Be and Li ions are mostly forward scattered while H and He ions are producing essential dose halo laterally and downstream of the Bragg peak. It is worth to mention that the maximum of deposited energy from H, B and He ions is slightly shifted forward in comparison to the Bragg Peak of primary C ions.

3.2. Characterisation of the ΔE–E telescope response in-field

Fig. 6 shows the positions (A–O) along the 290 MeV/u ^{12}C ion beam Bragg Peak, where the ΔE–E telescope was set.

The coincident signals from the ΔE and E detectors in response to the 290 MeV/u ^{12}C beam were mapped in a two dimensional (2D) scatter plot as ΔE vs ΔE + E. Fig. 7 shows the simulated 2D (ΔE, E + ΔE) scatter plots at positions A, C, I, J, K, L, which correspond to 0 mm, 58 mm, 128.5 mm, 129.5 mm, 130 mm and 131.5 mm depths within the PMMA phantom. The ΔE–E detector was placed along the central axis of the beam. It can be seen that at 0 mm depth in the phantom, 290 MeV/u ^{12}C

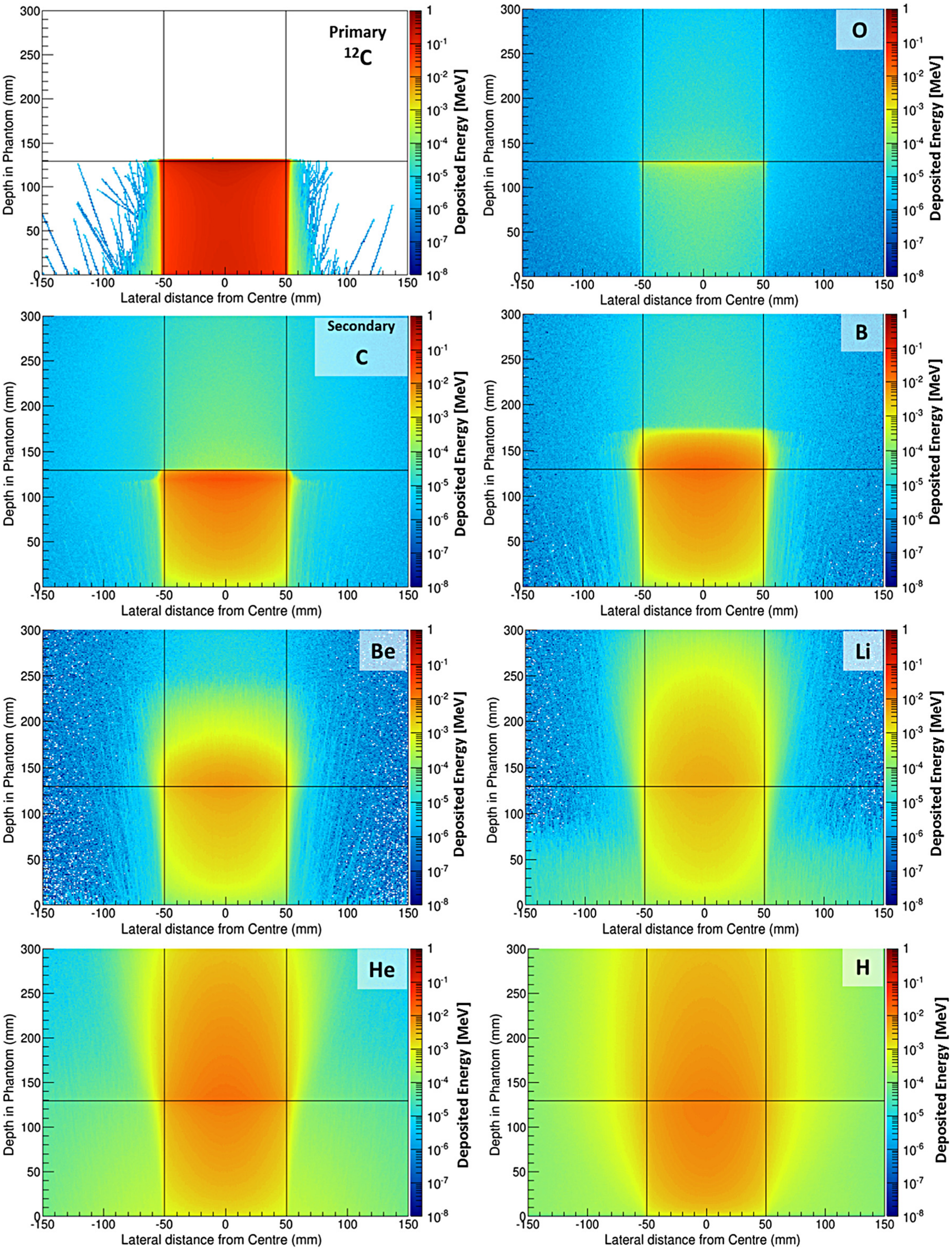

Fig. 5. 2D energy deposition map of primary and secondary particles in the PMMA phantom for HIMAC experiment setup. The results are shown per incident particle.

ions completely traversed the *Δ*E and E stages. The majority of energy events deposited in the E stage ranged between 11 and 13 MeV. Events occurred in *Δ*E stage are due to electrons which are travelling essentially along the *Δ*E detector and then scattered to E detector. The events along horizontal line depositing approximately 0.01–0.02 MeV in the *Δ*E stage are due to primary ^{12}C ions crossing through the *Δ*E and E stage of the detector under different angles.

At a depth of 58 mm in the PMMA phantom, the energy deposition regions corresponding to B, Be, Li, He, H fragments are clearly visible in the scatter plot.

At 128.5 mm depth in the PMMA phantom, the loci corresponding to fragmentation products are clearly observed. The maximum energy deposited in the E stage is about 185 MeV, which corresponds to the energy of ^{12}C ion having a range in silicon equal to the thickness of E

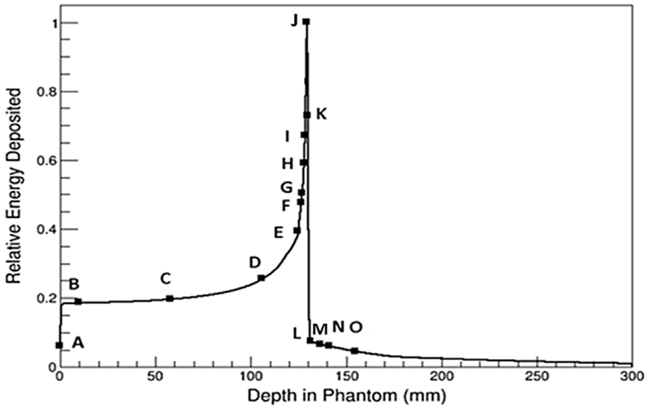

Fig. 6. A–O points indicate the positions along the 290 MeV/u ^{12}C Bragg Peak where the ΔE–E telescope was set.

stage of 500 µm. The energy deposited in the ΔE stage for 185 MeV ^{12}C ion is approximately 0.4 MeV. Events on a scatter plot on the left of the kink with an increased energy deposited in ΔE stage are corresponding to stoppers in the E stage. The most frequent energy deposition events occur between 80 and 100 MeV in the E stage which means that the majority of primary carbon ions are crossers as this depth while straggled essentially. The loci corresponding to oxygen and nitrogen were observed and corresponded to particles produced by inelastic reactions when ^{12}C ions interacted with the PMMA phantom.

The 2D energy scatter plot simulated in the ΔE–E telescope placed at the pinnacle of the Bragg peak (position J at 129.5 mm) is shown in Fig. 7. While most primary C ions are stoppers in E stage some of the C ions are still crossers due to increased straggling at the end of the range.

At 130 mm depth, the C ion locus is without a lower part of the kink due to all ^{12}C ions stopping within the E stage with a maximum energy of 2.4 MeV in the ΔE stage. Multiple loci that corresponded to the detection of different types of fragmented ions such as B, Be, Li, He, H were clearly seen. At a depth of 131.5 mm the contribution of all fragmentation was still observed These results show that in principle the ΔE–E detector is suitable for ^{12}C ion beam radiation field characterisation with high

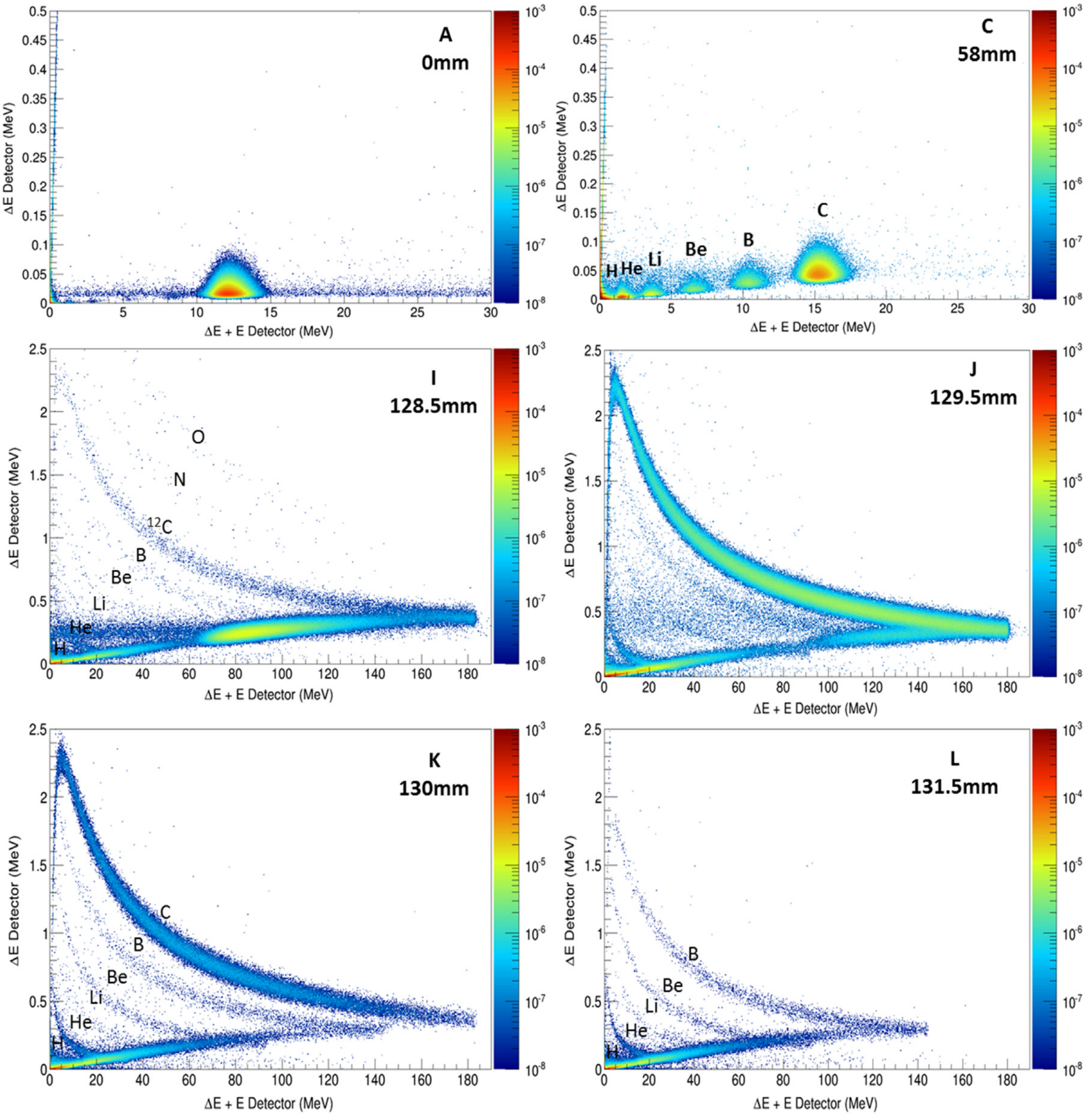

Fig. 7. Response of ΔE–E telescope to 290 MeV/u ^{12}C ion at depths 0, 58, 128.5, 129.5, 130, 131.5 mm in the PMMA phantom (two-dimensional ΔE–E plot). The results are shown per incident particle.

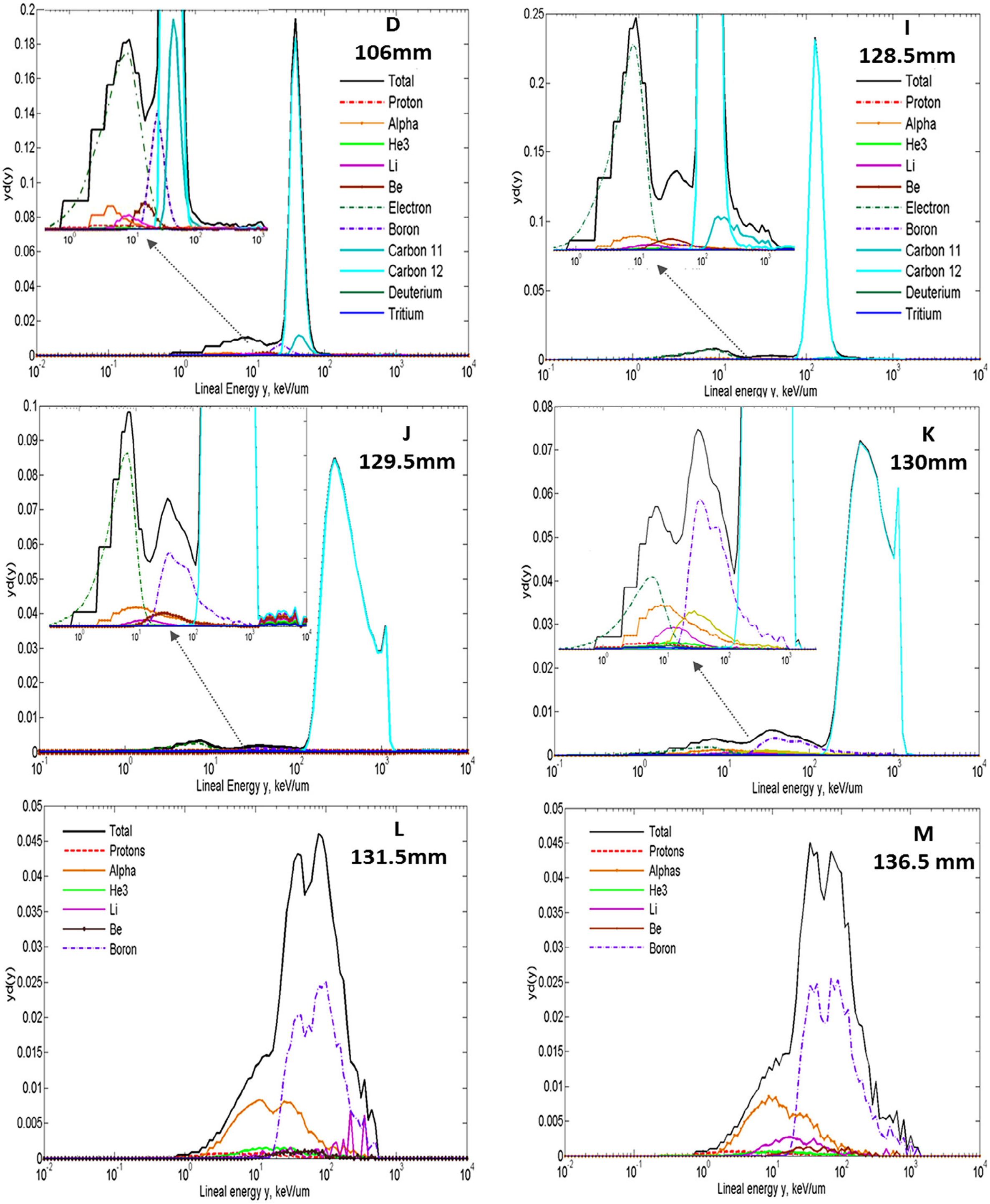

Fig. 8. Microdosimetric spectra derived from the *ΔE* stage at positions D, I, J, K, L and M. Separated dose weighted components have been shown in each microdosimetric spectrum.

spatial resolution in the distal edge of the Bragg peak providing accurate information at what depth the deposited energy is due to fragments only.

The microdosimetric spectra in silicon (with area normalised to 1) measured by *ΔE* stage in response to 290 MeV/u ^{12}C ion beam for depths of 106, 128.5, 129.5, 130 and 131.5 mm in the PMMA phantom are shown in Fig. 8.

At all depths up to 130 mm, the dose weighted contribution from ^{12}C ions was dominated with a clear shifting of ^{12}C microdosimetric spectrum to the region of higher lineal energies and spreading, due to the ^{12}C ion energy decreasing and ^{12}C ion scattering and the energy straggling are increasing with depth.

The other dose weighted partial microdosimetric spectra with lineal energies lower than 100 keV/μm, are corresponding to nuclear fragments such as B, Be, Li, ^{3}He, alpha particles and protons.

At a further depth in the PMMA phantom close to the distal part of the Bragg Peak (128.5 mm), a separate sharp peak occurs for the ^{12}C dose weighted microdosimetric spectra which corresponds to ^{12}C ions stopping in the *ΔE* stage and having range of 1.8 μm which is equal to the thickness of the *ΔE* stage. This peak is more pronounced 0.5 mm further downstream at 130 mm due to an increasing number of

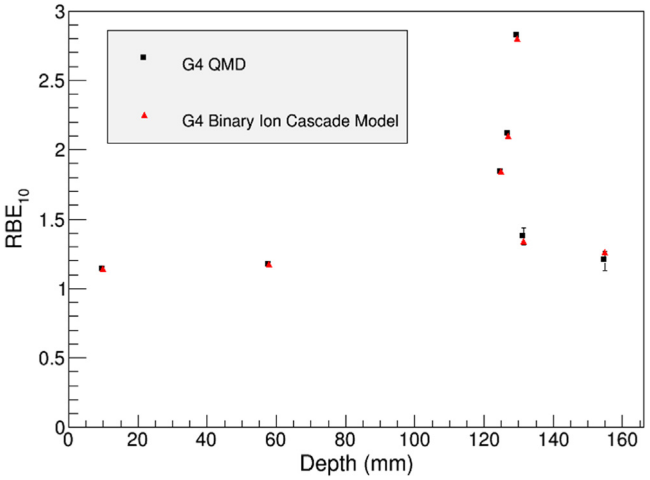

Fig. 9. RBE_{10} calculated adopting in the simulation the Geant4 Binary Ion Cascade and, alternatively, the QMD model, to describe ion hadronic interactions.

^{12}C ions with decreased energy at the very distal part of the BP. These detailed results demonstrate the capability of the silicon microdosimeter to obtain extremely high spatial resolution measurements, which were impossible with a TEPC, but which are crucial in determining the RBE accurately within the target tumour and beyond.

An interesting feature of the microdosimetric spectra is a partial dose weighted microdosimetric spectra peak corresponding to electrons. This peak is originated by scattered delta electrons from ^{12}C ions. These electrons have energies below approximately 600 keV which is calculated using the formula:

$$E_{\text{electrons}} = (4m_e/M_{\text{ion}}) \cdot E_{\text{ion}}, \tag{5}$$

where m_e is the mass of electron, M_{ion} is the mass of carbon ions and E is the energy of the ^{12}C ion. This peak is absent in the microdosimetric spectra at depth downstream of the Bragg peak that confirmed the origination of this peak.

Measurements of microdosimetric spectra at depth 131.5 mm (just behind of the Bragg peak) and 136.5 mm along the distal part of the Bragg Peak shown in Fig. 8 indicated that primary ^{12}C ions were not part of this mixed radiation field, although the contribution from fragments remains significant, with the largest dose weighted contribution deriving from B ions and alpha particles.

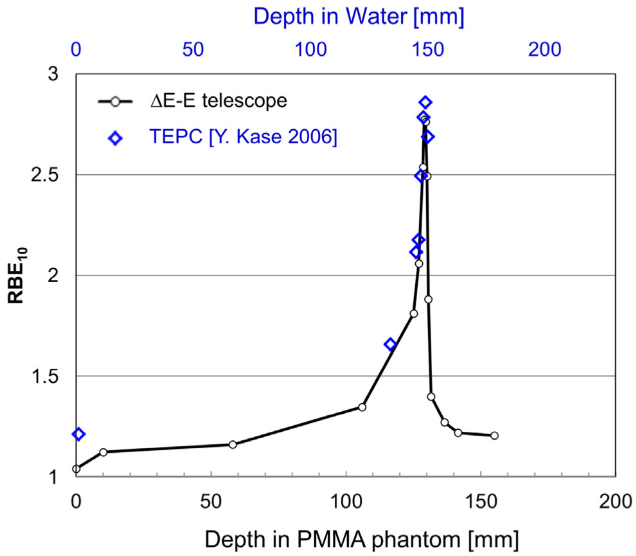

Fig. 10. Derived RBE_{10} along the central axis of the ^{12}C ion pristine BP, obtained by the ΔE stage. The RBE_{10} derived from measured values of y^* [21] are shown by blue rotated square.

3.3. RBE derivation by the ΔE–E telescope in ^{12}C ion beam

Using the microdosimetric spectra obtained by the ΔE stage in response to 290 MeV/u ^{12}C pristine BP for various depths in the PMMA phantom, the dose-mean lineal energy at each depth was obtained. The microdosimetric spectra have been converted from silicon to tissue using a conversion factor derived in [20].

The QGSP_BIC_HP physics list and the Quantum Molecular Dynamic (QMD) were used as alternative hadronic physics approaches to describe ion hadronic interactions. This strategy was adopted to evaluate the impact of alternative Geant4 physics models when calculating the RBE_{10}, by means of the MK model applied on the simulation microdosimetric results. Fig. 9 shows the RBE_{10} profiles obtained with the two alternative physics models. The RBE_{10} values derived using the two models agreed well with one another within 0.3 ± 0.03% in the proximal part of the BP, 0.7 ± 0.09% at the BP and 3.6 ± 1% in downstream of the BP.

The RBE_{10} profiles calculated using the MK model obtained by means of the Geant4 simulation and experimentally using a TEPC are shown

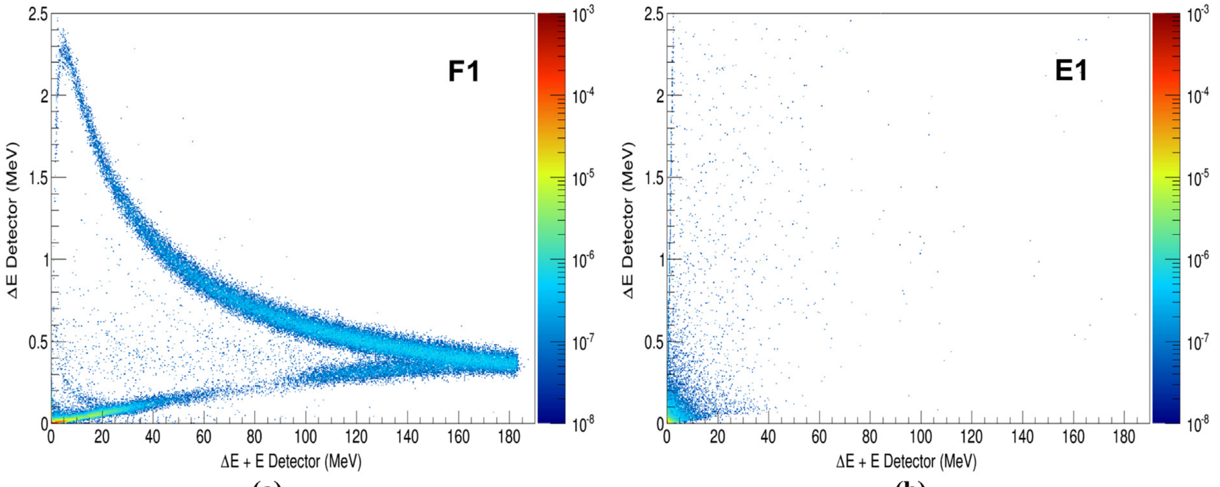

(a)

(b)

Fig. 11. Response of the telescope detector when positioned out-of-field at 0 mm. 20×10^6 events were simulated for both face on (F1) and edge on (E1) configurations. The results are shown per incident particle.

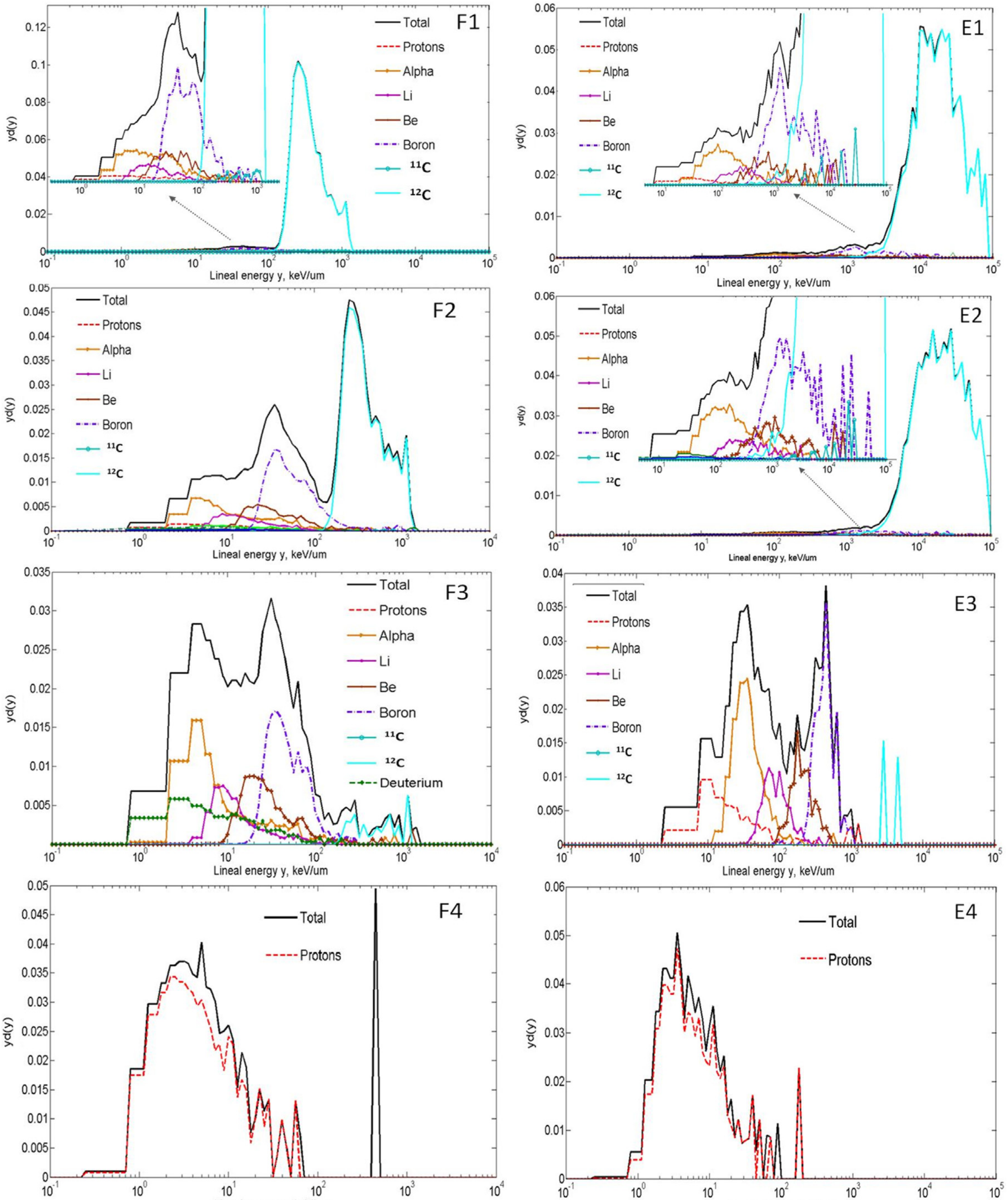

Fig. 12. Microdosimetric spectra derived from the *ΔE* stage in out of field study at 0 mm, 2 mm, 7 mm and 47 mm from the edge of the beam the Bragg peak. Separated components are shown in each microdosimetric spectrum.

in Fig. 10. The maximum derived RBE_{10} found using the 1.8 μm thick *ΔE* stage was approximately 2.8. The derived RBE_{10} profile, obtained by the *ΔE* stage agrees well with the profile which was also calculated with MK model using microdosimetric spectra measured by a TEPC at NIRS, Japan [21], however a discrepancy was observed at an entrance depth where the TEPC was placed at 1 mm depth in water as presented in [21] and the *ΔE*–E telescope was positioned at 0 mm depth in the PMMA phantom. This was due to the fact that the effective depth of the TEPC in water was actually 7.8 mm including the thickness of an A150 wall (1.27 mm), an Al shell (0.178 mm) and physical size of the TEPC spherical volume (12.7 mm). It should be noted that the *ΔE*–E telescope was measured in a PMMA phantom while the TEPC measurements were carried out in water, hence range scaling has been used to match the results.

3.4. Characterisation of ΔE–E telescope response out of field

Fig. 11 shows the response of the *ΔE*–*E* telescope when the device was placed out-of-field laterally in two configurations: face on (0°) and edge on (90°) (see Fig. 3). In the face on configuration there was a clear loci that could distinguish different species of particles (Fig. 11(a)) while the edge on configuration revealed a very different 2D energy scatter plot with an absence of clear loci (Fig. 11(b)); this result indicated the preferable forward directionality of the out-of-field charged ion

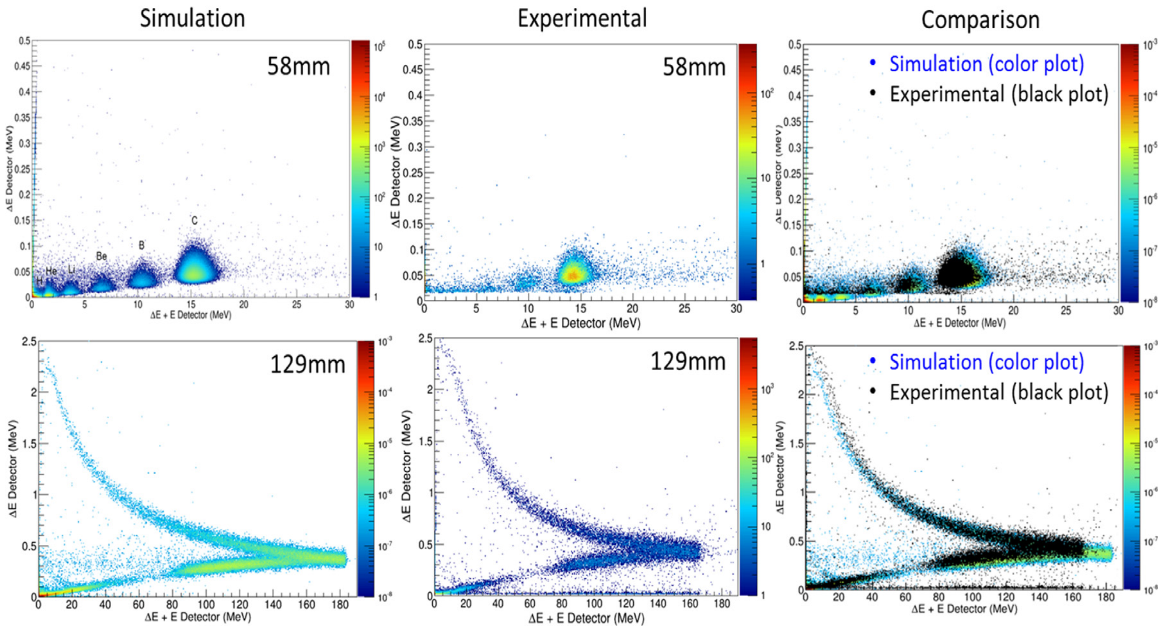

Fig. 13. Comparison of the simulated and experimental response of the ΔE–E telescope, at the 290 MeV/u ^{12}C ion HIMAC therapeutic beam.

components. The direction of the primary and secondary charged ions out-of-field can be seen in Fig. 5. The absence of loci was due to the long path length of the particles coming through the ΔE stage in edge-on configuration. The observed scatter plot on Fig. 11(b) is mostly due to delta electrons. Using ΔE–E telescope with pixelated ΔE stage provided cylindrical well defined SVs that will minimise the directional effect of the ΔE stage used in microdosimetric mode, however, for identification of particles, the ΔE–E telescope should be in a face on positioning relative to the primary beam direction.

Fig. 12 shows the microdosimetric spectra obtained by the ΔE stage when the detector was placed face on at 0 mm, 2 mm, 7 mm, and 47 mm laterally from the edge of the beam (positions F1, F2, F3 and F4), respectively, and edge on at positions E1, E2, E3 and E4 (see Fig. 3). When the ΔE–E telescope was placed at 0 mm from the edge of the beam and the surface of the detector is facing the beam (F1 position), there was a significant contribution to the microdosimetric spectra from ^{12}C ions that formed the penumbra region of the beam. Fragmentation products were also observed with lineal energies between a few keV/μm and 100 keV/μm, with the largest contribution coming from B ions. It is interesting that the dose weighted contribution from electrons was negligible due to lack of delta electrons originating from scattered Carbon ions in the penumbra region. At 2 mm from the edge of the beam (position F2), the partial dose weighted contribution of the ^{12}C ions was reduced while the contribution from fragments such as B, Be, Li, He, H increased. At 7 mm from the edge of the beam (position F3) almost all ^{12}C ions disappeared at this lateral depth but the fragments still remained significant due to the sharp penumbra of the ^{12}C ion beam. At a further lateral depth of 47 mm, only protons which corresponded to the combination of fragmented and recoil protons generated from neutron interactions in PMMA were observed.

A second alignment was carried out with the detector positioned in edge on configuration (positions E1, E2, E3 and E4). Here more energy was deposited in the ΔE stage from ions travelling parallel to the side of the ΔE–E detector. This caused a shift of microdosimetric spectra to the higher lineal energies observed in E1–3 plots of Fig. 12, when a chord length of 1.8 μm was used. This shift was clearer at positions closer to the field because nuclear fragments have a preferential forward scattering angular trajectory from the originating ion, while the path along the ΔE detector was 1 mm long.

The microdosimetric spectra at 47 mm obtained by detector in edge on and face on configurations are similar with most contribution from the protons originated by neutron elastic interactions in the phantom with an isotropic distribution. A much closer agreement in the microdosimetric spectra for positions F4 and E4 confirmed that the fragmented and neutron recoil proton fields were more isotropic than other heavier fragmented ions that were scattered mostly along the beam. The results showed that the microdosimetric spectra obtained by the ΔE stage of the monolithic telescope can give a detailed insight of the characteristics of the out of field beam. Certainly the microdosimetric spectra presented for positions E1–3 should not be considered as radiobiologically relevant because of the reasons cited above.

3.5. *Comparison to experiment in HIMAC, Japan*

Fig. 13 shows the experimental and the simulated response of the ΔE–E telescope to 290 MeV/u ^{12}C ions in the PMMA phantom at 58 mm and 129 mm for the HIMAC beam line. At (58±1) mm a good agreement is observed between experimental measurements and simulation results. At (129±1) mm depth in the PMMA phantom, the maximum energy deposited in the E stage in the experiment was about 160 MeV which is less than expected energy deposition in 500 μm of Si calculated by the Geant4 simulation. This discrepancy can be explained by the plasm a effect when high LETT ^{12}C ions hit the E stage and produce dense electron–hole pairs called plasma a columns. This leads too a strong columnar recombination before drift charge collection is dominated because the electric field in depleted E stage was not high enough. However, it can be clearly seen that the transmitted ^{12}C ions which have lower LET than ^{12}C stoppers deposited the same energy as simulated starting from approximately 80 MeV in both experimental and simulation results which supports the assumption that the E stage is 500 μm thick and the charge deficit is due to phenomena described above.

4. Conclusion

The characterisation of the ^{12}C ion beam at the HIMAC facility was studied in detail using Geant4. The 2D histogram of secondary charged particles provides very useful information about the distributions and directions of different ions of the mixed field.

The response of the ΔE–E telescope to 290 MeV/u ^{12}C ion beam at various depths in the PMMA phantom at HIMAC facility was investigated theoretically and experimentally. The RBE$_{10}$ values obtained by the ΔE–E telescope were found to be in good agreement with values obtained using a TEPC. Due to the high spatial resolution of the 1.8 μm thick ΔE stage, more detailed measurements were obtained at the end of the Bragg Peak compared to the TEPC. One limitation affecting the reported comparison is that the TEPC measurements were carried out in water which lacks the carbon component in contrast to PMMA.

It has been demonstrated that using the silicon to tissue conversion factor one can convert the microdosimetric spectra from silicon to tissue.

This study demonstrated that the ΔE–E silicon telescope can be used to characterise the mixed radiation field produced by the ^{12}C therapeutic beam. It is also possible to simultaneously measure the microdosimetric spectra with high spatial resolution, which is not currently achievable using TEPCs. The microdosimetric spectra then can also be used to determine the RBE_{10} of the radiation field by means of the MK model.

The ΔE–E telescope can be used to improve the Quality Assurance of existing treatment planning systems used in Heavy Ion Therapy and Geant4 benchmarking.

This study showed that adopting the G4IonBinaryCascade or, alternatively, the Geant4 QMD model does not have a significant impact on the calculation of the RBE_{10}.

Good agreement has been observed between simulation and experimental results, however a more in depth, systematic, quantitative comparison is foreseen as a next stage of the project, to quantify the accuracy of the Geant4 simulation model, using alternative hadronic physics models for ions. The experimental results concerning the response of the monolithic and pixelated ΔE–E telescope in the 290 MeV/u ^{12}C ion beam at HIMAC will be presented in more detail in a future paper.

Acknowledgements

This research was supported by the Australian Government through the Australian Research Council's Discovery Projects funding scheme (project DP 170102273).

We would like to thank the University of Wollongong Information Technology Services (ITS) for computing time on the UOW High Performance Computing Cluster and the research centre for charge particle therapy, National Institute of Radiological Science, Japan for providing valuable ^{12}C ion beam.

References

[1] H. Bethe, Theory of the passage of fast corpuscular rays through matter, Ann. Phys. 397 (1930) 325–400.

[2] F. Bloch, Bremsvermogen von Atomen mit mehreren Elektronen, Z. Phys. 81 (1933) 363–376.

[3] PART III. Particles and radiation therapy. Third International Conference, Int. J. Radiat. Oncol. Biol. Phys. 8 (1982).

[4] N. Matsufuji, T. Kanai, N. Kanematsu, T. Miyamoto, M. Baba, T. Kamada, H. Kato, S. Yamada, J.E. Mizoe, H. Tsujii, Specification of carbon ion dose at the National Institute of Radiological Sciences (NIRS), J. Radiat. Res. 48 (Suppl.) (2007) A:A81–A:A86.

[5] Rossi, M. Zaider, Microdosimetry and its Applications, Springer, London, 1996.

[6] Y. Kase, T. Kanai, M. Sakama, Y. Tameshige, T. Himukai, H. Nose, N. Matsufuji, Microdosimetric approach to NIRS-defined biological dose measurement for carbon-ion treatment beam, J. Radiat. Res. (ISSN: 0449-3060) 52 (1) (2011) 59–68.

[7] A.B. Rosenfeld, Novel detectors for silicon based microdosimetry their concepts and applications, Nucl. Instrum. Methods Phys. Res. A 809 (2016) 156–170.

[8] E. Haettner, H. Iwase, M. Krämer, G. Kraft, D. Schardt, Experimental study of nuclear fragmentation of 200 and 400 MeV/u ^{12}C ions in water for applications in particle therapy, Phys. Med. Biol. 58 (2013) 8265. http://dx.doi.org/10.1088/0031-9155/58/23/8265.

[9] H. Matsumoto, H. Koshiishi, T. Goka, M. Fujii, M. Hareyama, N. Kajiwara, S. Kodaira, K. Sakurai, N. Hasebe, Delta E × E silicon telescope of energetic heavy ions trapped in radiation belts, Japan. J. Appl. Phys. 1 44 (9A) (2005) 6870–6872.

[10] A.J. Kordyasz, E. Nossarzewska-Orlowska, E. Piaseckic, D. Lipiński, A. Brzozowski, J. Kownacki, M. Kowalczyk, Ł. Świderski, A. Syntfeld, L. Reissig, A. Pietrzaa, A. Jakubowski, R. Pozoreka, R. Gąsiorowski, Response to heavy ions and fission fragments of the monolithic silicon E–delta E telescopes produced by the quasiselective epitaxy, Nucl. Instrum. Methods Phys. Res. A 530 (1–2) (2004) 87–91.

[11] L.T. Tran, L. Chartier, D.A. Prokopovich, M.I. Reinhard, M. Petasecca, S. Guatelli, M.L.F. Lerch, V.L. Perevertaylo, M. Zaider, N. Matsufuji, M. Jackson, M. Nancarrow, A.B. Rosenfeld, 2014 3D-Mesa "Bridge" silicon microdosimeter: Charge collection study and application to RBE studies in ^{12}C radiation therapy, IEEE Trans. Nucl. Sci. 62 (2) (2015) 504–511.

[12] S. Agosteo, P.G. Fallica, A. Fazzi, M.V. Introini, A. Pola, G. Valvo, A pixelated silicon telescope for solid state microdosimetry, Radiat. Meas. 43 (2008) 585–589.

[13] Andrew Wroe, Reinhard Schulte, Alberto Fazzi, Andrea Pola, Stefano Agosteo, Anatoly Rosenfeld, Direct RBE estimation of radiation fields using a δE-E telescope, Med. Phys. 36 (10) (2009) 4486–4494.

[14] Linh T. Tran, Lachlan Chartier, David Bolst, Alex Pogossov, Susanna Guatelli, Dale A. Prokopovich, Marco Petasecca, Michael L.F. Lerch, Mark I. Reinhard, Benjamin Clasie, Nicolas Depauw, Hanne Kooy, Jay Flanz, Aimee McNamara, Harald Paganetti, Chris Beltran, Keith Furutani, Vladimir L. Perevertaylo, Michael Jackson, Anatoly B. Rosenfeld, Characterisation of proton pencil-beam scanning using a high spatial resolution solid state microdosimeter, Med. Phys. (2017). http://dx.doi.org/10.1002/mp.12563.

[15] Geant4 Collaboration, Geant4 User's Guide for Application Developers, 2012.

[16] ICRU 1989 tissue substitutes in radiation dosimetry and measurement, Report 44 of the International Commission on Radiation Units and Measurements.

[17] J. Allison, et al., Geant4 Collaboration, Geant4 developments and applications, IEEE Trans. Nucl. Sci. 53 (1) (2006) 270–278.

[18] NIST, National Institute of Standards and Technology PSTAR Database Program. http://physics.nist.gov/cgi-bin/Star/compos.pl?ap.

[19] J.F. Ziegler, SRIM, 2008. [Online] Available: http://www.srim.org.

[20] D. Bolst, S. Guatelli, L.T. Tran, L. Chartier, M. Lerch, N. Matsufuji, A. Rosenfeld, Correction factors to convert microdosimetry measurements in silicon to tissue in ^{12}C ion therapy, Phys. Med. Biol. 62 (6) (2017) 2055–2069.

[21] Y. Kase, T. Kanai, Y. Matsumoto, Y. Furusawa, H. Okamoto, T. Asaba, M. Sakama, H. Shinoda, Microdosimetric measurements and estimation of human cell survival for heavy-ion beams, Radiat. Res. 166 (4) (2006) 629–638.